materials

MDPI

Article

Effect of Sulfide and Chloride Ions on Pitting Corrosion of Type 316 Austenitic Stainless Steel in Groundwater Conditions Using Response Surface Methodology

Jin-Seok Yoo †, Nguyen Thuy Chung †, Yun-Ho Lee, Yong-Won Kim and Jung-Gu Kim *

Department of Materials Science and Engineering, Sungkyunkwan University, 2066, Seobu-Ro, Jangan-Gu, Suwon-Si 16419, Republic of Korea; wlstjr5619@skku.edu (J.-S.Y.); chung.ngthuy@g.skku.edu (N.T.C.); yunho0228@naver.com (Y.-H.L.); dyddnjs98@skku.edu (Y.-W.K.)

* Correspondence: kimjg@skku.edu

† These authors contributed equally to this work.

Abstract: This study investigates the corrosion resistance of Type 316 stainless steel as a candidate material for radioactive waste disposal canisters. The viability of stainless steel is examined under groundwater conditions with variations in pH, bisulfide ions (HS^-), and chloride ions (Cl^-) concentrations. Utilizing response surface methodology, correlations between corrosion factors and two crucial response variables, passive film breakdown potential and protection potential, are established. Cyclic potentiodynamic polarization tests and advanced analytical techniques provide detailed insights into the material's behavior. This research goes beyond, deriving an equation through response surface methodology that elucidates the relationship between the factors and breakdown potential. HS^- weakens the passive film and reduces the pitting corrosion resistance of the stainless steel. However, this study highlights the inhibitory effect of HS^- on pitting corrosion when Cl^- concentrations are below 0.001 M and at equivalent concentrations of HS^-. Under these conditions, immediate re-passivation occurs from the destroyed passive film to metal sulfides such as FeS_2, MoS_2, and MoS_3. As a result, no hysteresis loop occurs in the cyclic polarization curve in these conditions. This research contributes to the understanding of Type 316 stainless-steel corrosion behavior, offering implications for the disposal of radioactive waste in geological repositories.

Keywords: spent nuclear fuel; disposal canister; stainless steel; response surface methodology; soil corrosion

Citation: Yoo, J.-S.; Chung, N.T.; Lee, Y.-H.; Kim, Y.-W.; Kim, J.-G. Effect of Sulfide and Chloride Ions on Pitting Corrosion of Type 316 Austenitic Stainless Steel in Groundwater Conditions Using Response Surface Methodology. *Materials* **2024**, *17*, 178. https://doi.org/10.3390/ma17010178

Academic Editor: Xin-Yun Wang

Received: 6 December 2023
Revised: 24 December 2023
Accepted: 26 December 2023
Published: 28 December 2023

1. Introduction

Nuclear power stands out as a crucial energy resource in the battle against climate change due to its minimal carbon emissions. However, the disposal of radioactive spent nuclear energy, a byproduct of nuclear power generation, presents a formidable challenge. This waste, with half-lives extending from 10,000 to 1,000,000 years, demands secure storage deep underground with geologically stable conditions for prolonged periods [1,2]. Although disposal canisters for spent nuclear fuel are shielded by backfill materials and isolated from the soil environment, groundwater infiltration may occur after a long period of time [3]. Therefore, the canister materials need to be corrosion-resistant to withstand long-term exposure to the groundwater environment.

Numerous studies have identified that copper, Ni alloys, and Ti alloys are suitable materials for disposal canisters [4–6]. Notably, research in Sweden and Finland delves into copper canisters, while research in the United States has focused on Ni alloys and Ti alloys [7]. Although stainless steel is also a material with excellent corrosion resistance and high strength, it was evaluated as unsuitable for a spent nuclear fuel canister. This oversight is attributed to its vulnerability to localized corrosion in soil environments. Previous research has shown that sulfur, which originates from the oxidation of pyrite in the host

rock and sulfate-reducing bacteria in soil environments, could enhance localized corrosion of austenitic stainless steels in the presence of chloride ions (Cl^-) [7–10]. Furthermore, Lee et al. reported that hydrogen sulfide ions, so-called bisulfide ions (HS^-) were found to generate defective and less resistive passive film on Type 316L stainless steel [11,12].

However, A. Elbiache and P. Marcus reported that molybdenum (Mo) could improve the resistance to sulfur of Fe-Cr-Ni-Mo alloys in sulfuric acid conditions [13]. Additionally, Akiko et al. demonstrated that Mo could prevent localized corrosion of Ni-Cr-Mo-Fe alloys by producing a molybdenum sulfide passive film with cation selectivity in the NaCl and H_2S environments [14]. Recent research by Xiao et al. indicated that sulfur ions (S^{2-}) enhanced the re-passivation ability of 2205 duplex stainless steel and prevented pitting corrosion in the NaCl solution with the high pH [15].

According to the SKB-TR-10-67 report, when the canister was closed and the bentonite used as backfill was saturated (up to 100 years, oxygen existed), the values of pH, HS^- and Cl^- in the groundwater were expected to be 6.8–8, 0–1.3 mM, and 0.05–0.25 M, respectively [16]. Therefore, unlike previous studies, this research aims to explore the corrosion behavior of Type 316 stainless steel and the effects of pH, HS^-, and Cl^- under weak alkaline conditions with very low concentrations in groundwater.

To achieve this, response surface methodology (RSM) is used in this study. It is a highly efficient statistical analysis method that is useful for finding the relationship between several factors and one or more responses with a reasonable number of experiment designs [17]. Additionally, RSM can be used to generate a meaningful quadratic model to help predict the localized corrosion of stainless steel. In this study, RSM was employed to discern the relationship between the three corrosion factors (pH, HS^-, and Cl^-) and two response variables: the passive film breakdown potential (E_{break}) and the protection potential (E_{prot}) of stainless-steel Type 316 (UNS S31600) [18–20]. Cyclic Potentiodynamic Polarization tests (CPP) were utilized to obtain the two response variables, and the experiment with the three factors was designed using the Box-Behnken design (BBD) to model E_{break} and E_{prot}. Additionally, X-ray photoelectron spectroscopy (XPS) and cyclic voltammetry (CV) were conducted to analyze the passivation film concerning the corrosion factors.

2. Materials and Methods

2.1. Specimen Preparation

In this study, commercial-grade stainless steel Type 316, rolled to a thickness of 500 μm, was utilized. The chemical composition of the specimens is presented in Table 1. Before all electrochemical testing, the specimens underwent polishing with Si-C paper ranging from grit 220 to 600 [21]. This step ensured uniformity among the specimens, establishing a standardized surface for testing. The exposed surface area of each specimen was precisely adjusted to 1 cm^2 using silicon paste.

Table 1. Chemical composition of Type 316 stainless steel (wt.%).

Specimens	Composition (wt.%)									
	C	**Cr**	**Ni**	**Mo**	**Mn**	**P**	**S**	**Si**	**N**	**Fe**
Type 316	0.02	16.5	10.2	2.2	1.4	0.02	0.001	0.5	0.04	Bal.

2.2. Design of Experiments for Response Surface Methodology

RSM, a modern statistical and mathematical technique, was employed to model the response variables influenced by multiple factors. This study aimed to investigate how three factors, namely pH (A), log[HS^-] (B), and log[Cl^-] (C), influence the response variables E_{break} and E_{prot} under groundwater conditions. The BBD was chosen for the experiment matrix design due to its efficiency when dealing with three factors. Minitab (Minitab 19, Minitab, LLC., State College, PA, USA) and Statistita (Statistita v10, Stasista, Hamburg, Germany) software were used for the design of experiments and statistical analysis [22].

To ensure a comprehensive investigation, this study focused on three factors: pH and concentrations of HS^- and Cl^-. Table 2 outlines the ranges of pH and concentrations of HS^- and Cl^- examined in this study [23]. To simplify the adjustment and accuracy of the solutions, concentrations of HS^- and Cl^- were converted to a logarithmic scale. For statistical calculations, variables were coded using the minimum, medium, and maximum points of each variable separately, with values of −1, 0, and 1, respectively. The number of experiments was determined using the formula $N = k^2 + k + c_p$, where k represents the number of factors, 3, and c_p represents the number of experiments running at the center point, 3 [24]. The schematic of the design of experiments is illustrated in Figure 1 and Table 3, including 3 repeated center points and 12 different points [17]. Therefore, the total number of experiments to be conducted (N) was 15. Then, through the BBD results, a quadratic regression model can be created as shown in Equation (1).

$$Y = \beta_0 + \sum_{i=1}^{n} \beta_i X_i + \sum_{i=1}^{n} \beta_{ii} X_i^2 + \sum_{\substack{i,j=1 \\ i \neq j}}^{n} \beta_{ij} X_i X_j \quad (1)$$

where Y is the response, β_0 is a constant coefficient, β_i, β_{ii}, and β_{ij} are linear, quadratic, and interaction coefficients, respectively, and X_i and X_j are the coded values of the variables [24]. Responses were set to E_{break} and E_{prot}, and the model quality was confirmed by analysis of variance (ANOVA).

Table 2. The investigated value range of factors in this study.

Investigated Factor	A, pH	B, log[HS^- (mM)]	C, log[Cl^- (M)]
Investigated range	8 to 10	−2 to 0	−3 to −1

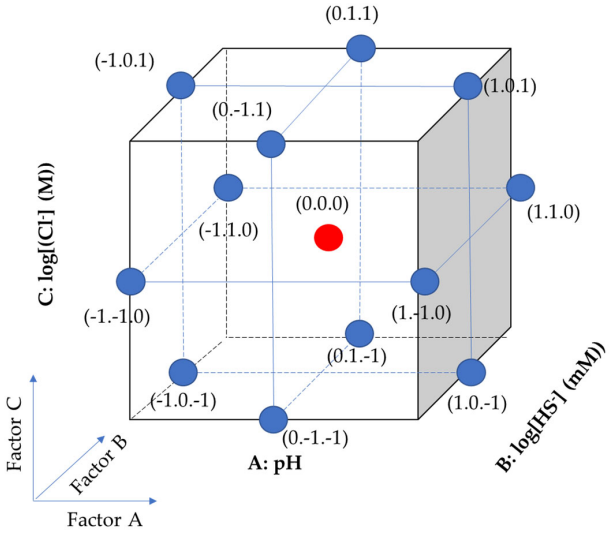

Figure 1. Schematic of BBD using this study.

Table 3. Experiments are designed based on BBD.

Standard Run	Coded Parameter			Real Parameter		
	A	B	C	pH	HS^- (mM)	Cl^- (M)
1	−1	−1	0	8	0.01	0.01
2	−1	0	−1	8	0.1	0.001
3	−1	0	1	8	0.1	0.1
4	−1	1	0	8	1	0.01
5	0	−1	−1	9	0.01	0.001

Table 3. *Cont.*

Standard Run	Coded Parameter			Real Parameter		
	A	B	C	pH	HS^- (mM)	Cl^- (M)
6	0	−1	1	9	0.01	0.1
7	0	0	0	9	0.1	0.01
8	0	1	−1	9	1	0.001
9	0	1	1	9	1	0.1
10	1	−1	0	10	0.01	0.01
11	1	0	−1	10	0.1	0.001
12	1	0	1	10	0.1	0.1
13	1	1	0	10	1	0.01
14	0	0	0	9	0.1	0.01
15	0	0	0	9	0.1	0.01

2.3. Electrochemical Tests

Electrochemical tests, including CPP and CV, were conducted using a three-electrode method in a 1000 mL Pyrex glass cell. The specimens were connected to the working electrode, while a saturated calomel electrode (SCE) served as the reference electrode, and two glassy carbons were employed as the counter electrode. The experimental medium was distilled water, with HS^- concentration controlled using Na_2S and Cl^- concentration controlled with NaCl. pH was adjusted using a 1 M sodium hydroxide solution and a saturated boric acid solution. All electrochemical tests were conducted using a VSP-300 instrument (Bio-Logic SAS, Seyssinet-Pariset, France) at 23 °C. The experiments included an open-circuit potential (OCP) for 24 h, and CPP scans started from 0 V vs. OCP with a rate of 0.166 mV/s. The back scan was initiated when the current density reached 0.1 mA/cm^2 at the same rate. Surface images of all specimens were collected for comparative analysis using an optical microscope (OM), and for the 0.001 M Cl^- conditions, additional pitting information was collected using a confocal laser scanning microscope (CLSM). CV tests were also employed with OCP for 24 h, and the scan was repeated from −1.7 V_{SCE} to 0.7 V_{SCE} with a rate of 50 mV/s for 30 cycles. The solutions used for CV were pH 8, 1 mM HS^-, and 0.1 M Cl^- and pH 8, 0.01 mM HS^-, and 0.1 M Cl^-.

2.4. XPS Analysis

XPS analysis was performed to analyze the chemical composition of the passive film after immersion for 24 h in different concentrations of HS^-. The solutions used for XPS analysis were also the same with CV tests (pH 8, 1 mM HS^-, and 0.1 M Cl^- and pH 8, 0.01 mM HS^-, and 0.1 M Cl^-). XPS analysis was carried out using an ESCA system (AXIS SUPRA, Kratos, Manchester, UK) with a monochromatic Al Kα radiation source (photoelectron energy of 1486.6 eV). High-resolution spectra were recorded in increments of 0.1 eV with a pass energy of 20 eV. The binding energies of the elements were calibrated to the carbon 1 s orbital at 284.8 eV.

3. Results and Discussion

3.1. Cyclic Polarization Measurements

To accurately determine the type of sulfur present in the solution, an understanding of the dissociation of H_2S in aqueous solutions is essential. The reactions and equilibrium equations in the solution are as follows [11,15]:

$$H_2S = HS^- + H^+, K_{a1} \quad (2)$$

$$HS^- = S^{2-} + H^+, K_{a2} \quad (3)$$

$$C_{Na_2S} = C_{H_2S} \times (1 + {}^{K_{a1}}/_{C_{H^+}} + K_{a1} \times {}^{K_{a2}}/_{C_{H^+}{}^2}) \quad (4)$$

Sun et al. suggested approximate values of K_{a1} and K_{a2} for Equations (2) and (3) at room temperature to be 10^{-7} mol/L and 10^{-12}–10^{-19} mol/L, respectively [25]. Considering the pH range of 8–10 in this study, the concentration of H_2S can be negligible because it is approximately 11 to 10^3 times lower than the concentration of Na_2S according to Equation (4), and the dissociation of HS^- is also negligible because of very low K_{a2}. Thus, it was assumed that the concentration of HS^- used in this study was equivalent to the concentration of dissolved Na_2S.

Figure 2a–c depict the cyclic polarization curves with the designed experiment BBD according to the concentration of Cl^- and the parameters of the results of CPP are presented in Table 4. The surfaces of the specimens after CPP were measured using OM and CLSM, as shown in Figures S1 and S2. An important point in surface observation after CPP is that no pitting was found under No. 8 experiments (pH 9, HS^- 1 mM, Cl^- 0.001 M).

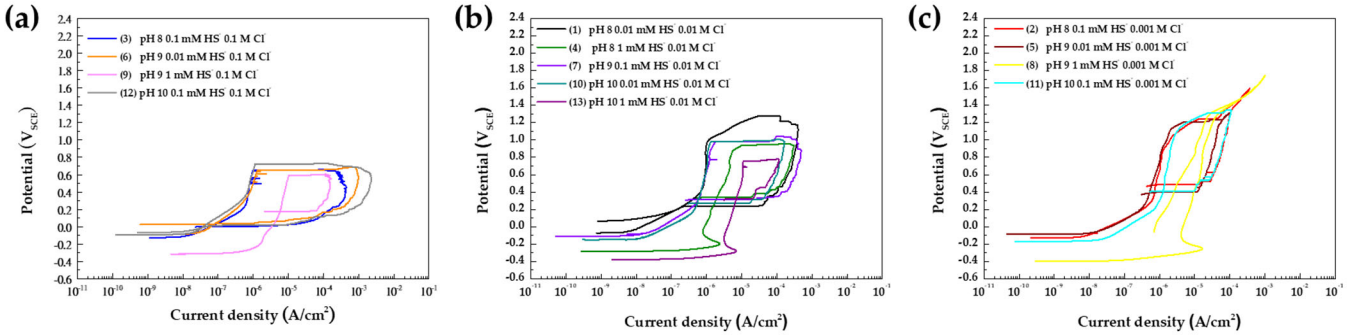

Figure 2. Cyclic polarization curves of Type 316 in the BBD according to the concentration of Cl^- (**a**) 0.1 M, (**b**) 0.01 M, and (**c**) 0.1 M.

Table 4. The results of the CPP are based on BBD.

Run	pH	HS^- (mM)	Cl^- (M)	E_{OCP} (mV_{SCE})	i_{pass} ($\mu A/cm^2$)	E_{break} (mV_{SCE})	E_{prot} (mV_{SCE})
1	8	0.01	0.01	−64	1.14	999	227
2	8	0.1	0.001	−126	12.96	1238	483
3	8	0.1	0.1	−121	0.99	652	42
4	8	1	0.01	−313	10.19	942	339
5	9	0.01	0.001	−79	5.09	1209	389
6	9	0.01	0.1	29	1.32	649	33
7	9	0.1	0.01	−86	1.79	982	312
8	9	1	0.001	−398	39.6	1263	1263
9	9	1	0.1	−313	10.23	593	177
10	10	0.01	0.01	−144	1.33	984	271
11	10	0.1	0.001	−168	24.22	1310	409
12	10	0.1	0.1	−83	1.14	725	−11
13	10	1	0.01	−373	11.03	758	323
14	9	0.1	0.01	−108	2.14	1022	213
15	9	0.1	0.01	−176	2.53	1052	257

E_{break} values were selected at the point where the current density sharply increased within the passive region (<1 V_{SCE}), while E_{break} reaching the transpassive region (>1 V_{SCE}) was considered the point where the anodic curve's slope changed. The current density at the E_{break} was set to the passive current density (i_{pass}). Additionally, during the back scan, the point where the polarization curve intersects was defined as E_{prot}. Regression models for E_{break} and E_{prot} were created and analyzed through ANOVA based on the results in Table 4.

3.2. Quadratic Regression Model and Analysis of Variance

The response variable, E_{break}, was analyzed using Minitab 19 software to obtain a quadratic regression model as shown below:

$$E_{break}\ (mV_{SCE}) = -1200 + 358{\cdot}pH + 139{\cdot}\log[HS^-] - 389{\cdot}\log[Cl^-] - 22.6{\cdot}pH^2 - 75.3{\cdot}(\log\ [HS^-])^2 \\ -14.8{\cdot}(\log\ [Cl^-])^2 - 42.2{\cdot}pH{\cdot}\log[HS^-] + 0.2{\cdot}pH{\cdot}\log[Cl^-] - 27.5{\cdot}\log[HS^-]{\cdot}\log[Cl^-] \quad (5)$$

The statistical significance of Equation (5) should be assessed through the F-test and *p*-value [26]. The ANOVA results and coefficient of determination (R^2) are presented in Table 5. ANOVA was employed to examine the relationship between the response variables and predictor variables. Generally, the significance level (α) was set to 0.05, and if the *p*-value of the regression model is less than α, it suggests that the model is statistically significant. In this model, the obtained F-value from the F-test was 15.39, exceeding the traditional threshold of $F_{critical}$ ($F_{(9,\ 5,\ 0.05)}$ = 4.77), and the *p*-value was below 0.05. Therefore, the model can reject the null hypothesis, which means that all coefficients are zero ($\beta_1 = \beta_2 = \beta_3 = \beta_{11} = \beta_{22} = \beta_{33} = \beta_{12} = \beta_{13} = \beta_{23} = 0$) and the model is statistically significant. However, only variables with T-values outside the range of $T_{critical}$ ($T_{(5,\ 0.05)}$ = 2.75) are meaningful, and the results in Table 5 reveal that only the variable log[Cl^-] (C) is significant in this model. Additionally, the R^2 (pred.) value is only 48.54%, indicating that the model has an overfitting problem.

Table 5. Results of the ANOVA of Equation (5) for predicting E_{break}.

ANOVA $F_{critical}$ ($DF_{regression}$, $DF_{residual}$, α) (9, 5, 0.05) = 4.77					
Source	**Degree of Freedom (DF)**	**Adj. Sum of Square**	**Adj. Mean Square**	**F-Value**	***p*-Value**
Regression	9	763,514	84,835	15.39	0.004
Residual	5	27,564	5513		
Lack of fit	3	25,097	8366		
Pure error	2	2467	1233		
Total	14	791,078			
Coded Coefficient $T_{critical}$ ($DF_{residual}$, α) (5, 0.05) = 2.57					
Term	Coefficient	Standard Error Coefficient	T-value	*p*-value	Remark
Constant	1018.7	42.9	23.76	0.000	<0.05
A	−6.7	26.3	−0.26	0.807	
B	−35.6	26.3	−1.36	0.233	
C	−300.1	26.3	−11.43	0.000	<0.05
AA	−22.6	38.6	−0.58	0.584	
BB	−75.3	38.6	−1.95	0.109	
CC	−14.8	38.6	−0.38	0.717	
AB	−42.2	37.1	−1.14	0.307	
AC	0.2	37.1	0.01	0.995	
BC	−27.5	37.1	−0.74	0.492	
Summary Model					
R^2 = 96.52%		R^2 (adj.) = 90.24%		R^2 (pred.) = 48.54%	

To address non-significant variables, a systematic revision of the model was conducted by eliminating each non-significant variable. The detailed R^2 of revised Equations (5.1) and (5.6) summaries are provided in Table S1 of the supplementary section. The optimized Equation (6) was selected for the best model of E_{break} of the specimen.

$$E_{break}\ (mV_{SCE}) = 288.8 - 180.9{\cdot}\log[HS^-] - 300.1{\cdot}\log[Cl^-] - 72.7{\cdot}(\log\ [HS^-])^2 \quad (6)$$

With information from the optimized Equation (6) in Table 6, it is evident that the model has been significantly simplified and improved. The F-value is notably higher than $F_{critical}$ ($F_{(3,\ 11,\ 0.05)}$ = 3.59). Importantly, only one variable (B) is non-significant in this

refined model, according to the T-test. Notably, R^2 (pred.) exceeds 90%, while both R^2 and R^2 (adj.) remain higher than 90%, indicating a substantial improvement over the original model, and the model no longer exhibits signs of overfitting as observed previously.

Table 6. Results of the ANOVA of the revised Equation (6) for predicting E_{break}.

ANOVA $F_{critical}$ ($DF_{regression}$, $DF_{residual}$, α) (3, 11, 0.05) = 3.59					
Source	**Degree of Freedom (DF)**	**Adj. Sum of Square**	**Adj. Mean Square**	**F-Value**	***p*-Value**
Regression	3	750,464	250,155	67.75	0.000
Residual	11	40,614	19,710		
Lack of fit	9	38,147	4239		
Pure error	2	2467	1233		
Total	14	791,078			
Coded Coefficient $T_{critical}$ ($DF_{residual}$, α) (11, 0.05) = 2.20					
Term	Coefficient	Standard Error Coefficient	T-value	*p*-value	Remark
Constant	997.3	24.6	40.57	0.000	<0.05
B	−35.6	21.5	−1.66	0.125	
C	−300.1	21.5	−13.97	0.000	<0.05
BB	−72.7	33.7	−2.31	0.041	<0.05
Summary Model					
R^2 = 94.87%		R^2 (adj.) = 93.47%		R^2 (pred.) = 90.19%	

Figure 3a–c are response surfaces and contour lines from Equation (6). According to Equation (6) and Figure 3, E_{break} is entirely independent of pH and depends solely on Cl^- and HS^-. This result affirms that the neutral-to-slightly basic pH of groundwater environments does not affect E_{break}, aligning with previous studies [27,28]. Additionally, this model bears a striking resemblance to Strehblow and Titze's Equation (7), illustrating the relationship between E_{break} and aggressive ion concentrations [29].

$$E_{break}\ (mV_{SCE}) = A - B \cdot \log C_{agg} \quad (7)$$

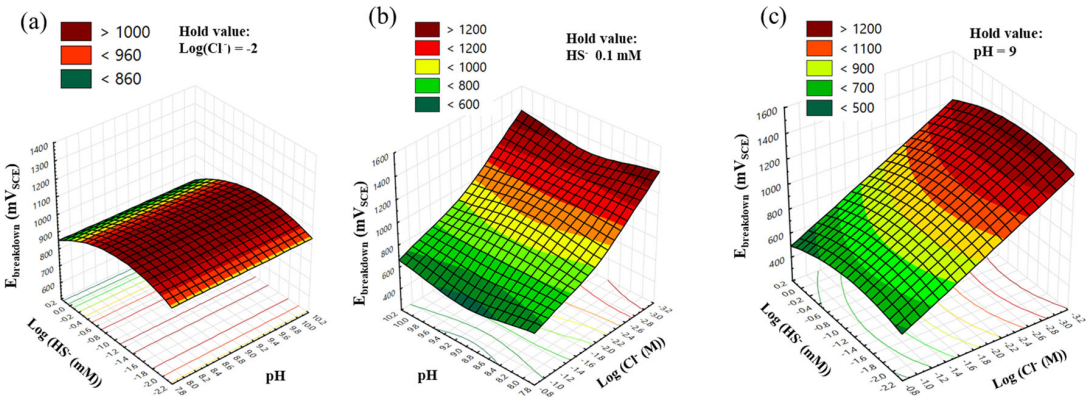

Figure 3. Response surfaces and contour plots from Equation (6) show the effect of (**a**) pH and log[HS^-], (**b**) pH and log[Cl^-], and (**c**) log[HS^-] and log[Cl^-] on the E_{break} of Type 316 stainless steel.

In Equation (7), A and B are constants, where B signifies the aggressiveness of the specific ions. In our study, Equation (6) exhibits similarities but introduces an additional quadratic term for HS^-. This implies that the relationship with log[HS^-] is not purely a negative linear effect, as observed with log[Cl^-] under the given conditions. The E_{break} attains its maximum value when the concentration of HS^- is 0.058 mM ($10^{-1.24}$ mM), as depicted in Figure 3c. However, given that the concentration of HS^- in groundwater is

significantly lower than the concentration of Cl^-, its influence appears unclear due to the dominating effect of Cl^-. Particularly when the concentration of Cl^- is 0.1 M, confirming the effect of HS^- on localized corrosion of the specimen becomes challenging, as illustrated in Figure 2a.

The impact of HS^- is evident in E_{prot}, which increased with a concentration of 1 mM HS^- at all Cl^- concentrations, as shown in Figure 4a–c and Table 4. To statistically analyze the change in E_{prot} by each factor, a regression model of E_{prot} was created. The model for E_{prot} is presented in Equation (8) and Table 7.

$$\begin{aligned} E_{prot}(mV_{SCE}) = {} & -8277 + 1832{\cdot}pH + 182{\cdot}\log[HS^-] - 226{\cdot}\log[Cl^-] - 102.7{\cdot}pH^2 + 132.0{\cdot}(\log[HS^-])^2 \\ & +72.8{\cdot}(\log[Cl^-])^2 - 15.0{\cdot}pH{\cdot}\log[HS^-] + 5.2{\cdot}pH{\cdot}\log[Cl^-] - 182.5{\cdot}\log[HS^-]{\cdot}\log[Cl^-] \end{aligned} \quad (8)$$

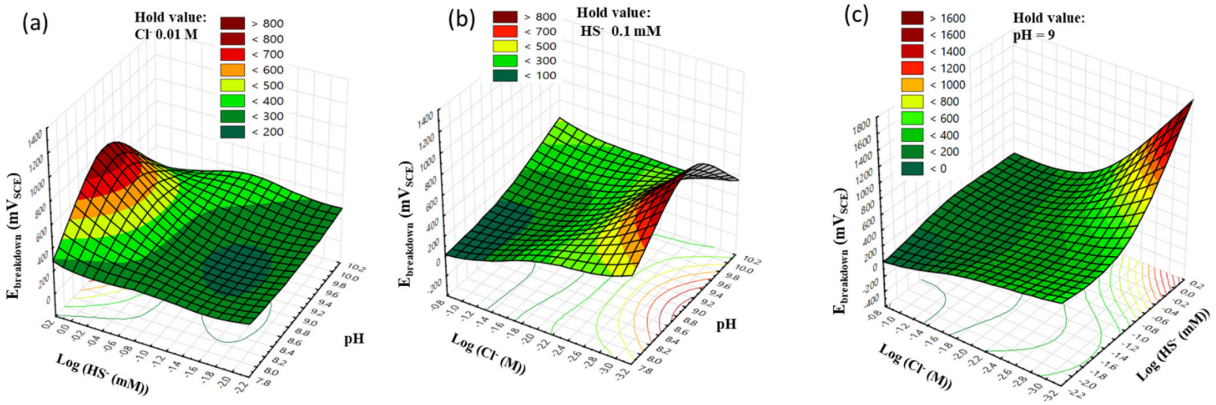

Figure 4. Response surfaces and contour plots from Equation (8) show the effect of (**a**) pH and log[HS^-], (**b**) pH and log[Cl^-], and (**c**) log[HS^-] and log[Cl^-] on the E_{prot} of Type 316 stainless steel.

Table 7. Results of the ANOVA of the revised Equation (8) for predicting E_{prot}.

ANOVA $F_{critical}$ ($DF_{regression}$, $DF_{residual}$, α) (9, 5, 0.05) = 4.77					
Source	**Degree of Freedom (DF)**	**Adj. Sum of Square**	**Adj. Mean Square**	**F-Value**	***p*-Value**
Regression	9	1,103,426	122,603	4.34	0.060
Residual	5	141,283	28,257		
Lack of fit	3	136,363	45,454		
Pure error	2	4921	2460		
Total	14	1,244,710			
Coded Coefficient $T_{critical}$ ($DF_{residual}$, α) (5, 0.05) = 2.57					
Term	Coefficient	Standard Error Coefficient	T-value	*p*-value	Remark
Constant	260.7	97.1	2.69	0.044	<0.05
A	−12.4	59.4	−0.21	0.843	
B	147.8	59.4	2.49	0.055	
C	−287.9	59.4	−4.84	0.005	<0.05
AA	−102.7	87.5	−1.17	0.293	
BB	132	87.5	1.51	0.192	
CC	72.8	87.5	0.83	0.443	
AB	−15	84	−0.18	0.865	
AC	5.3	84	0.06	0.953	
BC	−182.5	84	−2.17	0.082	
Summary model					
R^2 = 88.65%		R^2 (adj.) = 68.22%		R^2 (pred.) = 00.00%	

However, as listed in Table 7, the F-value in Equation (8) was lower than $F_{critical}$, while R^2 (pred.) was also 0, indicating that this model was not statistically significant and was under an overfitting problem. Despite attempts to optimize the model depicted in Table S2, this issue persisted. The overfitting can be attributed to the significant deviation observed

in experiment No. 8. In this experiment, with the same Cl^- concentration of 0.001 M (equivalent to 1 mM) and HS^- concentration, the polarization curve of the stainless steel did not even exhibit a hysteresis loop, suggesting that the specimen resisted pitting corrosion under these conditions. These results emphasize that HS^- is not exclusively an aggressive ion; it can act as an inhibitor, contributing to an increase in the resistance to pitting corrosion of the specimen, particularly when considering the ratio of HS^- concentration in the Cl^- condition.

3.3. Surface Analysis and Corrosion Mechanism

XPS analysis was performed to provide evidence of surface changes and clarify the effect on the passive film depending on the concentration of HS^-. Type 316 stainless steel is an Fe-Cr-Ni-Mo alloy, and Fe, Cr, and Mo can mainly affect the properties of the passivation film. The specimens used in the XPS analysis were immersed in 0.01 mM and 1 mM HS^- solutions for 24 h, with a fixed pH 8 and Cl^- concentration of 0.1 M, respectively. Figure 5a–f show the results of the XPS spectra of Cr 2p, Fe 2p, Mo 3d, O 1p, S 2s, 2p, and Ni 2p, respectively. Table 8 shows the binding energies of the primary compounds of the passive film obtained from XPS spectra deconvolution. The XPS spectra of Type 316 stainless steel showed no significant difference in its chemical compositions, even when the HS^- concentration changed. However, as the concentration of HS^- increased, the area fraction ratios of $Cr(OH)_3/Cr_2O_3$ and OH^-/O^{2-} increased, as shown in Table 9. Compared to Cr_2O_3, the content of $Cr(OH)_3$ in the passive film has less protective resistance and more defects [30,31]. Therefore, when the concentration of HS^- increases, the protection of the passivation film decreases, so that i_{pass} increases, as shown in Figure 2 and Table 4. On the other hand, when HS^- is present in the solution, Ni is not significantly affected, but Fe and Mo sulfides, such as FeS_2, MoS_2, and MoS_3, can be generated and act as a passive film, as shown in Figure 5b,c,e [32–34]. These results can also be confirmed through the Pourbaix diagram. The Pourbaix diagram of Fe-H_2O-S and Mo-H_2O-S systems presented by Davoodi et al. showed that FeS_2 and MoS_2 are stable phases in OCP measured in this study [35].

Table 8. Binding energies of the primary compounds of the passive film.

Element	Peak	Species (Binding Energy/eV)	Reference
Cr	2p3/2	Cr_{met} (573.6 ± 0.1); Cr_2O_3 (576.0 ± 0.1); $Cr(OH)_3$ (577.3 ± 0.1)	[36]
Mo	3d5/2	Mo_{met} (227.3 ± 0.1); Mo^{4+} (228.5 ± 0.1); Mo^{6+} (231.8 ± 0.1)	[37–39]
	3d3/2	Mo_{met} (230.5 ± 0.1); Mo^{4+} (232.9 ± 0.1); Mo^{6+} (234.8 ± 0.1)	
Fe	2p3/2	Fe_{met} (706.5 ± 0.1); FeS_2 (707.3 ± 0.1); Fe_3O_4 (709.5± 0.1); Fe_2O_3 (710.7 ± 0.1); FeOOH (711.8 ± 0.1); $Fe_2(SO_4)_3$ (713.0 ± 0.1)	[15,40,41]
O	1s	O^{2-} (529.9 ± 0.1); OH- (531.2 ± 0.1); H_2O (532.6 ± 0.1)	[42,43]
	2s	S^{2-} (225.8 ± 0.1)	
S	2p3/2	S^{2-} (161.2 ± 0.1); S_2^{2-} (162.8 ± 0.1); SO_4^{2-} (168.3 ± 0.1)	[44–47]
	2p1/2	S^{2-} (162.6 ± 0.1); S_2^{2-} (164.8 ± 0.1); SO_4^{2-} (169.6 ± 0.1)	
Ni	2p3/2	Ni_{met} (852.5 ± 0.1); NiO (853.7 ± 0.1)	[48]

Table 9. Area fraction ratio of deconvolted XPS spectra of passive film.

Concentration of HS^- (mM)	Area Fraction Ratio	
	$Cr(OH)_3/Cr_2O_3$	OH^-/O^{2-}
0.01	0.70	0.91
1	0.79	1.08

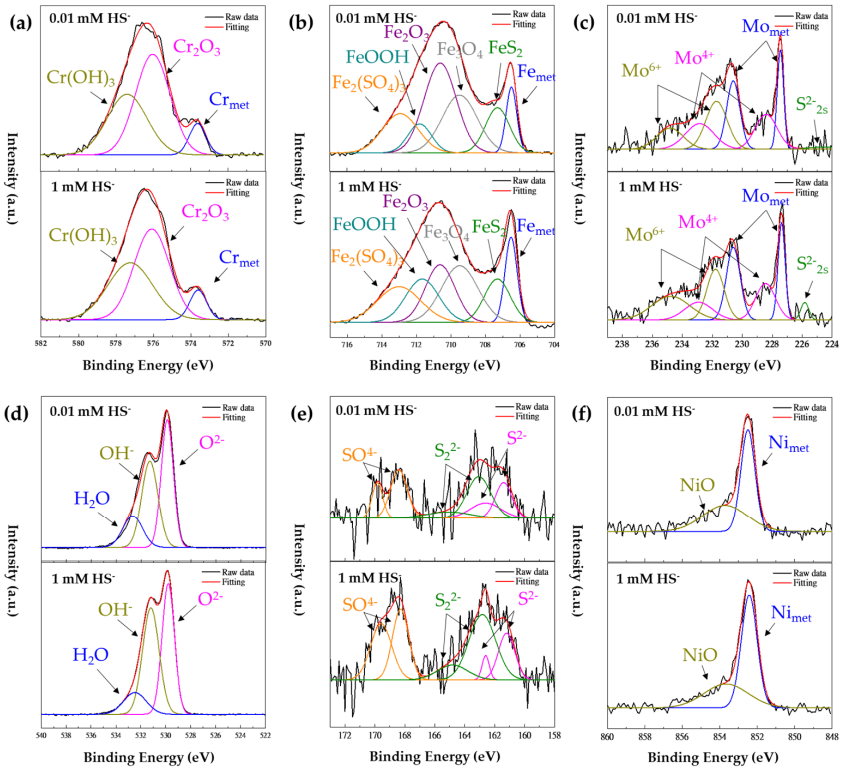

Figure 5. High-resolution scanning XPS spectra in different concentrations of HS^- (**a**) Cr 2p, (**b**) Fe 2p, (**c**) Mo 3d, (**d**) O 1s, (**e**) S 2p, and (**f**) Ni 2p.

Additionally, CV tests were performed for passive film analysis according to concentrations of HS^-, as depicted in Figure 6a,b. When CV was performed depending on the concentration of HS^-, a notable difference occurred in the oxidation peaks. Also, as the CV cycles were repeated, it was confirmed that the intensity of the peaks became more clear due to the metal ions eluted from the specimen. The peak I between −0.9 and −1.0 V_{SCE} indicates that Fe is oxidized to a Fe^{2+} ion, and the reduction peak of the reaction is displayed by peak I′. The pick II between −0.5 and −0.6 V_{SCE} indicates that the Fe^{2+} ion is oxidized to the Fe^{3+} ion, and the reduction peak of the reaction is represented by peak II′ [49]. The peak IV indicates that the Cr^{3+} ion is oxidized to the Cr^{6+} ion, and peak V indicates the cathodic reduction of dissolved oxygen [50]. The response of peak I depending on the concentration of HS^- is explained by the following equations [51].

$$Fe + HS^- \rightarrow Fe(HS)_{ads} + e^- \quad (9)$$

$$Fe(HS)_{ads} + OH^- \rightarrow FeS + H_2O + e^- \quad (10)$$

Then, Haleem et al. suggested that peak III (~0.189 V_{SCE}) also generated FeS_2 with the following equation [52].

$$Fe + 2HS^- + 2OH^- \rightarrow FeS_2 + 2H_2O + 4e^- \quad (11)$$

On the other hand, other studies suggested that the peaks III and III′ are the reactions of MoS_4^{2-} ions with the following equations [53,54].

$$MoS_4^{2-} \rightarrow MoS_3 + \frac{1}{8}S_8 + 2e^- \quad (12)$$

$$MoS_3 + \frac{1}{8}S_8 + 2e^- \rightarrow MoS_4^{2-} \quad (13)$$

$$MoS_4^{2-} + 2H_2O + 2e^- \rightarrow MoS_2 + 2HS^- + 2OH^- \quad (14)$$

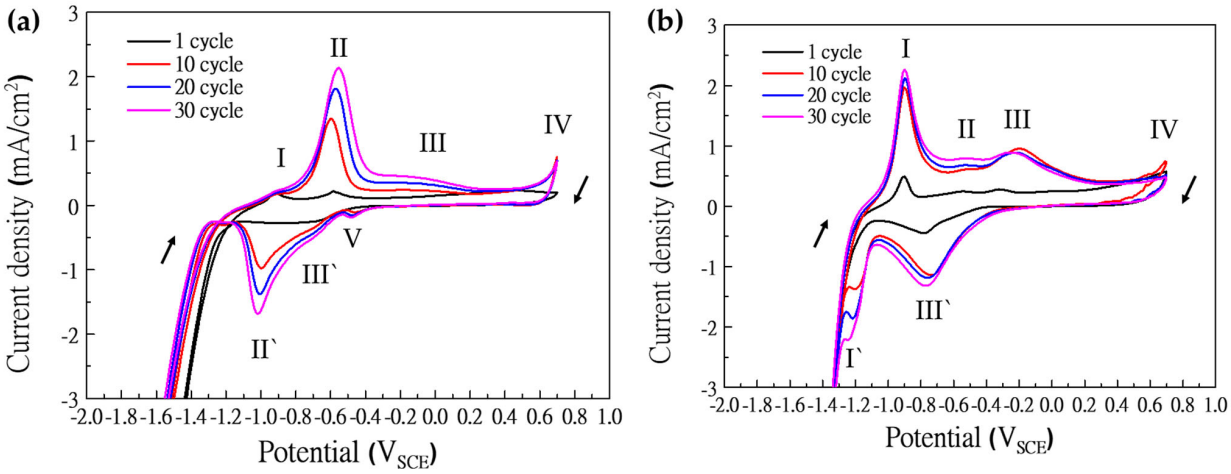

Figure 6. Results of CV according to concentration of HS^-: (**a**) 0.01 mM, and (**b**) 1 mM.

In peak III, MoS_3 is generated by Equation (12). On the other hand, the peak III′ overlaps the reduction reactions of Equations (13) and (14). First, the reduction reaction of MoS_3 occurs according to Equation (13), and then MoS_2, a new reductive deposition material, is generated according to Equation (14) below about −0.55 V_{SCE}.

Through XPS and CV analyses, it is clear that a new passive film is formed on the surface due to HS^-. The presence of HS^- leads to an increased ratio of OH^-/O^{2-}, causing the dense and stable Cr_2O_3 on the passive film to decrease and become more susceptible to destruction. However, conversely, the broken passive film on the surface is re-passivated into new materials such as FeS_2, MoS_2, and MoS_3 by the abundant HS^-. Particularly when the concentrations of Cl^- and HS^- were equal in the groundwater condition, it was confirmed that the destroyed passivation film immediately underwent re-passivation, providing resistance to the corrosion of Type 316 stainless steel. Additionally, as depicted in Figure 7, no hysteresis loop was observed in the specimens after conducting CPP under conditions of pH 8 and 10, 0.001 M Cl^-, and 1 mM HS^-. This indicates that the resistance to pitting corrosion of Type 316 stainless steel remains unaffected by pH under these specific mildly alkaline conditions.

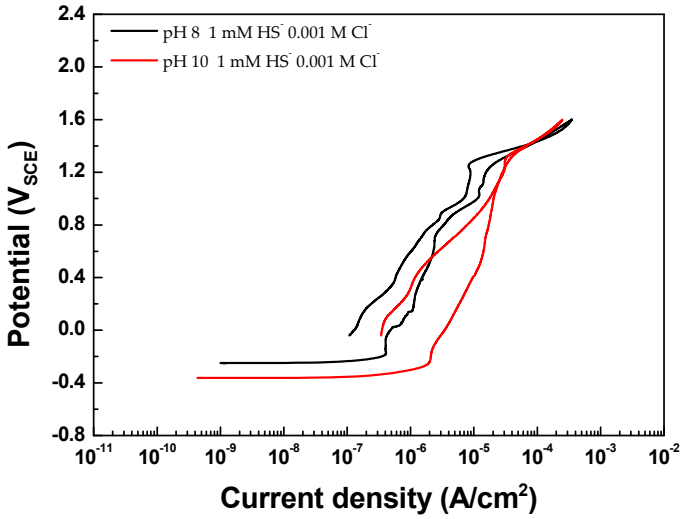

Figure 7. CPP curves according to pH 8 and 10 under 1 mM HS^- and 0.001 M Cl^- conditions.

4. Conclusions

This study aimed to assess the suitability of Type 316 stainless steel for spent nuclear fuel disposal canisters, employing statistical analysis to scrutinize the impact of pH, HS^-, and Cl^- on localized corrosion in groundwater. Key findings include:

- The concentrations of Cl^- and HS^- were significant factors affecting E_{break} on a logarithmic scale. Especially HS^- reduces the ratio of Cr_2O_3, which plays a crucial role in the passive film of stainless steel.
- On the other hand, HS^- reacts with Fe and Mo, the main components of the passive film on Type 316 stainless steel, forming new metal sulfides on the passive film and contributing to the re-passivation behavior of Type 316 stainless steel.
- Under specific conditions (Cl^- concentration 0.001 M, equal HS^- concentration), the alloy re-passivates the broken film immediately with metal sulfides (FeS_2, MoS_2, MoS_3), displaying resistance to pitting corrosion.
- Therefore, regardless of pH, Type 316 stainless steel exhibits no hysteresis loop in the cyclic polarization curve under these conditions, suggesting negligible localized corrosion concerns.

In conclusion, this study identifies critical Cl^- and HS^- concentrations, affirming Type 316 stainless steel's pitting resistance in weak alkaline groundwater with oxygen and holding valuable implications for its use in the disposal of radioactive waste in geological repositories.

Supplementary Materials: The following supporting information can be downloaded at: https://www.mdpi.com/article/10.3390/ma17010178/s1, Figure S1: Surface OM images of specimens after experiments under all CCP conditions; Figure S2. Surface CLSM images of specimens after experiments under 0.001 M Cl^- CCP conditions (a) pH 8, 0.1 mM HS^-, (b) pH 9, 0.01 mM HS^-, (c) pH 9, 1 mM HS^-, and (d) pH 10, 0.1 mM HS^-; Table S1. Summary revised Models E_{break} of Model (5); Table S2. Summary revised Models of E_{prot}.

Author Contributions: Conceptualization, J.-S.Y., N.T.C. and J.-G.K.; methodology, J.-S.Y., N.T.C., Y.-H.L. and Y.-W.K.; software, J.-S.Y. and N.T.C. validation, J.-S.Y., N.T.C. and J.-G.K. formal analysis, J.-S.Y. and N.T.C.; investigation, J.-S.Y. and N.T.C.; writing—original draft preparation, J.-S.Y. and N.T.C.; writing—review and editing, J.-G.K.; visualization, J.-S.Y., N.T.C. and Y.-H.L.; supervision, J.-G.K. All authors have read and agreed to the published version of the manuscript.

Funding: This work was supported by the Nuclear Research and Development Program of the National Research Foundation of Korea (NRF), funded by the Ministry of Science and ICT (MSIT) (NRF-2021M2E1A1085195).

Institutional Review Board Statement: Not applicable.

Informed Consent Statement: Not applicable.

Data Availability Statement: Data are contained within the article and supplementary materials.

Acknowledgments: This work was supported by the Nuclear Research and Development Program of the National Research Foundation of Korea (NRF), funded by the Ministry of Science and ICT (MSIT) (NRF-2021M2E1A1085195).

Conflicts of Interest: The authors declare no conflict of interest.

References

1. Ahn, T.M. Multiple lines of evidence for performance of the canister and waste form in long-term nuclear waste disposal: Reviews. *Prog. Nucl. Energy* **2016**, *93*, 343–350. [CrossRef]
2. Féron, D.; Crusset, D.; Gras, J.-M. Corrosion issues in nuclear waste disposal. *J. Nucl. Mater.* **2008**, *379*, 16–23. [CrossRef]
3. King, F.; Padovani, C. Review of the corrosion performance of selected canister materials for disposal of UK HLW and/or spent fuel. *Corros. Eng. Sci. Technol.* **2011**, *46*, 82–90. [CrossRef]
4. Ab, S.K. Long-term safety for the final repository for spent nuclear fuel at Forsmark. *Main Rep. SR Site Proj.* **2018**, *1*, 276.
5. Shoesmith, D. Assessing the corrosion performance of high-level nuclear waste containers. *Corrosion* **2006**, *62*, 703–722. [CrossRef]

6. Féron, D.; Crusset, D.; Gras, J.M. Corrosion issues in the French high-level nuclear waste program. *Corrosion* **2009**, *65*, 213–223. [CrossRef]
7. King, F. Container materials for the storage and disposal of nuclear waste. *Corrosion* **2013**, *69*, 986–1011. [CrossRef]
8. Newman, R.; Isaacs, H.; Alman, B. Effects of sulfur compounds on the pitting behavior of type 304 stainless steel in near-neutral chloride solutions. *Corrosion* **1982**, *38*, 261–265. [CrossRef]
9. Meguid, E.A.E.; Mahmoud, N.; Gouda, V. Pitting corrosion behaviour of AISI 316L steel in chloride containing solutions. *Br. Corros. J.* **1998**, *33*, 42–48. [CrossRef]
10. El Meguid, E.A.; Mahmoud, N.; El Rehim, S.A. The effect of some sulphur compounds on the pitting corrosion of type 304 stainless steel. *Mater. Chem. Phys.* **2000**, *63*, 67–74. [CrossRef]
11. Lee, J.-S.; Kitagawa, Y.; Nakanishi, T.; Hasegawa, Y.; Fushimi, K. Effect of hydrogen sulfide ions on the passive behavior of type 316L stainless steel. *J. Electrochem. Soc.* **2015**, *162*, C685. [CrossRef]
12. Lee, J.-S.; Kitagawa, Y.; Nakanishi, T.; Hasegawa, Y.; Fushimi, K. Passivation behavior of type-316L stainless steel in the presence of hydrogen sulfide ions generated from a local anion generating system. *Electrochim. Acta* **2016**, *220*, 304–311. [CrossRef]
13. Elbiache, A.; Marcus, P. The role of molybdenum in the dissolution and the passivation of stainless steels with adsorbed sulphur. *Corros. Sci.* **1992**, *33*, 261–269. [CrossRef]
14. Tomio, A.; Sagara, M.; Doi, T.; Amaya, H.; Otsuka, N.; Kudo, T. Role of alloyed molybdenum on corrosion resistance of austenitic Ni–Cr–Mo–Fe alloys in H_2S–Cl–environments. *Corros. Sci.* **2015**, *98*, 391–398. [CrossRef]
15. Xiao, Y.; Tang, J.; Wang, Y.; Lin, B.; Nie, Z.; Li, Y.; Normand, B.; Wang, H. Corrosion behavior of 2205 duplex stainless steel in NaCl solutions containing sulfide ions. *Corros. Sci.* **2022**, *200*, 110240. [CrossRef]
16. King, F.; Lilja, C.; Pedersen, K.; Pitkänen, P.; Vähänen, M. *An Update of the State-of-the-Art Report on the Corrosion of Copper under Expected Conditions in a Deep Geologic Repository*; Swedish Nuclear Fuel and Waste Management Co.: Stockholm, Sweden, 2010.
17. Kumari, M.; Gupta, S.K. Response surface methodological (RSM) approach for optimizing the removal of trihalomethanes (THMs) and its precursor's by surfactant modified magnetic nanoadsorbents (sMNP)—An endeavor to diminish probable cancer risk. *Sci. Rep.* **2019**, *9*, 18339. [CrossRef] [PubMed]
18. King, F.; Lilja, C.; Vähänen, M. Progress in the understanding of the long-term corrosion behaviour of copper canisters. *J. Nucl. Mater.* **2013**, *438*, 228–237. [CrossRef]
19. Chen, J.; Qin, Z.; Wu, L.; Noël, J.; Shoesmith, D. The influence of sulphide transport on the growth and properties of copper sulphide films on copper. *Corros. Sci.* **2014**, *87*, 233–238. [CrossRef]
20. Kursten, B.; Druyts, F. Methodology to make a robust estimation of the carbon steel overpack lifetime with respect to the Belgian Supercontainer design. *J. Nucl. Mater.* **2008**, *379*, 91–96. [CrossRef]
21. *ASTM G5-87*; Standard Reference Test Method for Making Potentiostatic and Potentiodynamic Anodic Polarization Measurements. ASTM International: West Conshohocken, PA, USA, 2010.
22. Behmaneshfar, A.; Sadrnia, A.; Karimi-Maleh, H. A Review of Different Types of DOE Methods as a Useful Platform for Improving the Performance of Nano Adsorbents in Removal Systems of Pollutants. *Nanosci. Nanotechnol.-Asia* **2020**, *10*, 219–227. [CrossRef]
23. Nguyen, T.C.; So, Y.-S.; Yoo, J.-S.; Kim, J.-G. Machine learning modeling of predictive external corrosion rates of spent nuclear fuel carbon steel canister in soil. *Sci. Rep.* **2022**, *12*, 20281. [CrossRef]
24. Chung, N.T.; So, Y.-S.; Kim, W.-C.; Kim, J.-G. Evaluation of the influence of the combination of ph, chloride, and sulfate on the corrosion behavior of pipeline steel in soil using response surface methodology. *Materials* **2021**, *14*, 6596. [CrossRef]
25. Sun, W.; Nešić, S.; Young, D.; Woollam, R.C. Equilibrium expressions related to the solubility of the sour corrosion product mackinawite. *Ind. Eng. Chem. Res.* **2008**, *47*, 1738–1742. [CrossRef]
26. Luo, X.; Bai, R.; Zhen, D.; Yang, Z.; Huang, D.; Mao, H.; Li, X.; Zou, H.; Xiang, Y.; Liu, K. Response surface optimization of the enzyme-based ultrasound-assisted extraction of acorn tannins and their corrosion inhibition properties. *Ind. Crops Prod.* **2019**, *129*, 405–413. [CrossRef]
27. Janik-Czachor, M. An assessment of the processes leading to pit nucleation on iron. *J. Electrochem. Soc.* **1981**, *128*, 513C. [CrossRef]
28. Soltis, J. Passivity breakdown, pit initiation and propagation of pits in metallic materials–review. *Corros. Sci.* **2015**, *90*, 5–22. [CrossRef]
29. Strehblow, H.-H.; Titze, B. Pitting potentials and inhibition potentials of iron and nickel for different aggressive and inhibiting anions. *Corros. Sci.* **1977**, *17*, 461–472. [CrossRef]
30. Lu, B.; Luo, J.; Lu, Y. Effects of pH on lead-induced passivity degradation of nuclear steam generator tubing alloy in high temperature crevice chemistries. *Electrochim. Acta* **2013**, *87*, 824–838. [CrossRef]
31. Guo, L.; Qin, S.; Yang, B.; Liang, D.; Qiao, L. Effect of hydrogen on semiconductive properties of passive film on ferrite and austenite phases in a duplex stainless steel. *Sci. Rep.* **2017**, *7*, 3317. [CrossRef]
32. Liu, H.; Hua, Y.; Shi, S.; Lin, X.; Neville, A.; Wang, Y.; Sun, J. Stability of passive film and pitting susceptibility of 2205 duplex stainless steel in CO_2/H_2S-containing geothermal environment. *Corros. Sci.* **2023**, *210*, 110832. [CrossRef]
33. Monnot, M.; Roche, V.; Estevez, R.; Mantel, M.; Nogueira, R.P. Molybdenum effect on the Sulfide Stress Corrosion of a super martensitic stainless steel in sour environment highlighted by Electrochemical Impedance Spectroscopy. *Electrochim. Acta* **2017**, *252*, 58–66. [CrossRef]
34. Wang, Z.; Feng, Z.; Zhang, L. Effect of high temperature on the corrosion behavior and passive film composition of 316 L stainless steel in high H_2S-containing environments. *Corros. Sci.* **2020**, *174*, 108844. [CrossRef]

35. Davoodi, A.; Pakshir, M.; Babaiee, M.; Ebrahimi, G.R. A comparative H_2S corrosion study of 304L and 316L stainless steels in acidic media. *Corros. Sci.* **2011**, *53*, 399–408. [CrossRef]
36. Eidhagen, J.; Larsson, A.; Preobrajenski, A.; Delblanc, A.; Lundgren, E.; Pan, J. Synchrotron XPS and Electrochemical Study of Aging Effect on Passive Film of Ni Alloys. *J. Electrochem. Soc.* **2023**, *170*, 021506. [CrossRef]
37. Maurice, V.; Peng, H.; Klein, L.H.; Seyeux, A.; Zanna, S.; Marcus, P. Effects of molybdenum on the composition and nanoscale morphology of passivated austenitic stainless steel surfaces. *Faraday Discuss.* **2015**, *180*, 151–170. [CrossRef]
38. Fu, J.; Yu, P.; Zhang, N.; Ren, G.; Zheng, S.; Huang, W.; Long, X.; Li, H.; Liu, X. In situ formation of a bifunctional interlayer enabled by a conversion reaction to initiatively prevent lithium dendrites in a garnet solid electrolyte. *Energy Environ. Sci.* **2019**, *12*, 1404–1412. [CrossRef]
39. Saha, D.; Patel, V.; Selvaganapathy, P.R.; Kruse, P. Facile fabrication of conductive MoS_2 thin films by sonication in hot water and evaluation of their electrocatalytic performance in the hydrogen evolution reaction. *Nanoscale Adv.* **2022**, *4*, 125–137. [CrossRef]
40. Wang, Z.; Hu, H.; Zheng, Y. Synergistic effects of fluoride and chloride on general corrosion behavior of AISI 316 stainless steel and pure titanium in H_2SO_4 solutions. *Corros. Sci.* **2018**, *130*, 203–217. [CrossRef]
41. Yao, J.; Jin, T.; Li, Y.; Xiao, S.; Huang, B.; Jiang, J. Electrochemical performance of $Fe_2(SO_4)_3$ as a novel anode material for lithium-ion batteries. *J. Alloys Compd.* **2021**, *886*, 161238. [CrossRef]
42. Gandla, S.; Gollu, S.R.; Sharma, R.; Sarangi, V.; Gupta, D. Dual role of boron in improving electrical performance and device stability of low temperature solution processed ZnO thin film transistors. *Appl. Phys. Lett.* **2015**, *107*, 152102. [CrossRef]
43. Zheng, X.; Li, P.; Zheng, S.; Zhang, Y. Thermal decomposition of ammonium perchlorate in the presence of $Cu(OH)_2{\cdot}2Cr(OH)_3$ nanoparticles. *Powder Technol.* **2014**, *268*, 446–451. [CrossRef]
44. Solís-Casados, D.A.; Escobar-Alarcón, L.; Klimova, T.; Escobar-Aguilar, J.; Rodríguez-Castellón, E.; Cecilia, J.A.; Morales-Ramírez, C. Catalytic performance of CoMo/Al_2O_3-MgO-Li (x) formulations in DBT hydrodesulfurization. *Catal. Today* **2016**, *271*, 35–44. [CrossRef]
45. Harish, S.; Bharathi, P.; Prasad, P.; Ramesh, R.; Ponnusamy, S.; Shimomura, M.; Archana, J.; Navaneethan, M. Interface enriched highly interlaced layered MoS_2/NiS_2 nanocomposites for the photocatalytic degradation of rhodamine B dye. *RSC Adv.* **2021**, *11*, 19283–19293. [CrossRef] [PubMed]
46. Yu, X.; Mei, J.; Du, Y.; Cheng, X.; Wang, X.; Wu, Q. Engineered interface of three-dimensional coralliform NiS/FeS_2 heterostructures for robust electrocatalytic water cleavage. *Nano Res.* **2023**. [CrossRef]
47. Gao, Y.; Li, Z.; Fu, Z.; Zhang, H.; Wang, G.; Zhou, H. Highly selective capacitive deionization of copper ions in FeS2@N, S co-doped carbon electrode from wastewater. *Sep. Purif. Technol.* **2021**, *262*, 118336. [CrossRef]
48. Chen, Z.; Dedova, T.; Acik, I.O.; Danilson, M.; Krunks, M. Nickel oxide films by chemical spray: Effect of deposition temperature and solvent type on structural, optical, and surface properties. *Appl. Surf. Sci.* **2021**, *548*, 149118. [CrossRef]
49. Cabrini, M.; Lorenzi, S.; Pastore, T. Cyclic voltammetry evaluation of inhibitors for localised corrosion in alkaline solutions. *Electrochim. Acta* **2014**, *124*, 156–164. [CrossRef]
50. Ferreira, M.; Silva, T.M.E.; Catarino, A.; Pankuch, M.; Melendres, C. Electrochemical and laser Raman spectroscopy studies of stainless steel in 0.15 M NaCl solution. *J. Electrochem. Soc.* **1992**, *139*, 3146. [CrossRef]
51. Liu, L.; Wang, M.; Wang, Z.; Zhang, Y. Corrosion behavior of 316L stainless steel anode in alkaline sulfide solutions and the consequent influence on Ga electrowinning. *Hydrometallurgy* **2015**, *157*, 285–291. [CrossRef]
52. El Haleem, S.A.; El Aal, E.A. Electrochemical behaviour of iron in alkaline sulphide solutions. *Corros. Eng. Sci. Technol.* **2008**, *43*, 173–178. [CrossRef]
53. Wang, Y.; Mayyas, M.; Yang, J.; Tang, J.; Ghasemian, M.B.; Han, J.; Elbourne, A.; Daeneke, T.; Kaner, R.B.; Kalantar-Zadeh, K. Self-Deposition of 2D Molybdenum Sulfides on Liquid Metals. *Adv. Funct. Mater.* **2021**, *31*, 2005866. [CrossRef]
54. Morales-Guio, C.G.; Hu, X. Amorphous molybdenum sulfides as hydrogen evolution catalysts. *Acc. Chem. Res.* **2014**, *47*, 2671–2681. [CrossRef] [PubMed]